Research Square

Preprints are preliminary reports that have not undergone peer review.
They should not be considered conclusive, used to inform clinical practice,
or referenced by the media as validated information.

# Synergistic effect between rare-earth and copper species enhances hydrothermal stability of Cu-SSZ-13 for NO abatement

**Liu Yang**
Baotou Research Institute of Rare Earths
**Yuanjiang Wang**
Baotou Research Institute of Rare Earths
**Tiantian Zhang**
Baotou Research Institute of Rare Earths
**Hao Qu**
Baotou Research Institute of Rare Earths
**Xin Guo**
Baotou Research Institute of Rare Earths
**Cheng Zhang**
Baotou Research Institute of Rare Earths
**Yan Wang**
Baotou Research Institute of Rare Earths
**Mi Yan**
Zhejiang University
**Pengfei Xie**
pfxie@zju.edu.cn

Zhejiang University

**Article**

**Keywords:** Rare-earth, Hydrothermal stability, Cu migration, Dual-atom catalyst, Theoretical guidance

**Posted Date:** April 1st, 2026

**DOI:** https://doi.org/10.21203/rs.3.rs-9227856/v1

**License:** This work is licensed under a Creative Commons Attribution 4.0 International License.
Read Full License

**Additional Declarations:** No competing interests reported.

# Synergistic effect between rare-earth and copper species enhances hydrothermal stability of Cu-SSZ-13 for NO abatement

*Liu Yang* [a, 1], *Yuanjiang Wang* [a, 1], *Tiantian Zhang* [a], *Hao Qu* [a], *Xin Guo* [a], *Cheng Zhang* [a], *Yan Wang* [a, *], *Mi Yan* [a, d], *and Pengfei Xie* [a, b, c *]

[a] State Key Laboratory of Baiyunobo Rare Earth Resource Researches and Comprehensive Utilization, Baotou Research Institute of Rare Earths, Baotou 014030, China

[b] Key Laboratory of Biomass Chemical Engineering of Ministry of Education, College of Chemical and Biological Engineering, Zhejiang University, Hangzhou 310058, China

[c] Institute of Zhejiang University-Quzhou, Quzhou 324000, China

[d] Zhejiang Province Key Laboratory of Advanced Information Materials, School of Materials Science and Engineering, Zhejiang University, Hangzhou 310058, China

[1] Liu Yang and Yuanjiang Wang contributed equally to this work.

* Corresponding Authors Email: pfxie@zju.edu.cn; wy_brire@brire.com.

**ABSTRACT**

Cu-SSZ-13 catalysts have been demonstrated with excellent performance for selective catalytic reduction of $NO_x$ with $NH_3$ ($NH_3$-SCR), but remain a great challenge to be stable after hydrothermal aging, specifically in the scenario of a hydrogen combustion engine exhaust containing high water partial pressure. Here, we employ first-principles computational calculations to screen a series of rare earth (RE) modified Cu-SSZ-13, to investigate the impact on the low-temperature activity after hydrothermal aging. An yttrium (Y)-doping Cu-SSZ-13 has been screened out and exhibits a catalytic temperature window (175~555 ℃) of ~100 ℃ wider than that of conventional Cu-SSZ-13 (182~464 ℃) after hydrothermal aging. The characterizations unveil that the incorporation of Y modulates the catalytic microenvironments, generating more active and stable copper species. Further crystal orbital Hamilton population and ab initio molecular dynamics calculations interpret that RE elements, especially Y, doped in 6MRs, induce charge redistribution of Cu cations in 8MRs, increase the barrier of aggregation, and ultimately enhance the hydrothermal stability. This study reveals a clear structure-stability relationship for RE-modified Cu-SSZ-13, paving the way for the next generation of $NH_3$-SCR catalysts used in hydrogen fuel engines.

*Keywords:* Rare-earth; Hydrothermal stability; Cu migration; Dual-atom catalyst; Theoretical guidance

## 1. Introduction

Hydrogen fuel generated in a water-splitting electrolyze are promising contributors to achieve zero carbon emissions of the internal combustion engine. Nevertheless, a catalytic aftertreatment system is still required to eliminate nitrogen oxides ($NO_x$) produced in the emission of hydrogen combustion engines, where $N_2$ and $O_2$ in the atmosphere are directly burned under high-temperature[1,2]. Among commercialization $NO_x$ aftertreatment systems, one of the most effective methods currently used is the ammonia selective catalytic reduction of $NO_x$ ($NH_3$-SCR) based on Cu-SSZ-13[3-7]. However, it still faces technical challenges. Particularly, the exhaust gas temperature is generally lower than in traditional engines especially under cold-start conditions, and the stream contains more water vapor, reaching up to 30 vol.%. Therefore, the improvement of low-temperature activity after hydrothermal treatment for Cu-SSZ-13 is significantly important.

It is well known that one of viable option to enhance the catalytic property is to introduce a secondary cation into Cu-SSZ-13 by tuning the distribution, activity, and stability of active component $Cu^{2+}$ ions, including $Z_2Cu$ located at the paired Al site and $ZCu(OH)^+$ at the single Al site (Z represents the negative framework charge)[8-15]. Among them, rare earth (RE) metal ions are the most attractive electronic modifiers, which can regulate the chemical natures of $Z_2Cu$ and $ZCu(OH)^+$, thereby endowing it with superior catalytic performance[12,16-18]. However, we find that although the incorporation of Ce modulates the catalytic microenvironments, generates more active $ZCu(OH)^+$ species, and creates more newly adsorptive sites for $NH_3$ and nitrate species than Cu-SSZ-13，resulting in higher low-temperature $NH_3$-SCR activity, it has a minor effect on hydrothermal stability[19]. And the systematic investigations on the structure-

activity relationships of different RE doping Cu-SSZ-13 catalysts after hydrothermal aging have not been reported to date, which leading to a grand challenge to optimize the compositional and structural properties at the atomic scale for the development of next-generation $NH_3$-SCR catalysts.

In this study, we employ a combined computational and experimental methodologies to gain intrinsic insights into the impact of diverse RE elements (La, Ce, Pr, Nd, Sm, Eu and Y) on the low-temperature activity of Cu-SSZ-13 after hydrothermal aging in SCR reaction. The first principles computational calculations identify promising candidates, and various experimental techniques are employed to assess the $NH_3$-SCR catalytic performance. Additionally, extensive control experiments offer profound insights into the catalytic microenvironments of dynamic Cu species, along with the underlying interaction mechanisms and reaction pathways. Moreover, Crystal Orbital Hamilton Population (COHP) calculations and the Ab Initio Molecular Dynamics (AIMD) simulations are utilized to reveal the influence of different RE elements on the deactivation mechanism of $ZCu(OH)^+$ and the effect of bond strength changes on the removal behavior of $ZCu(OH)^+$. This work is anticipated to offer valuable guidance for the design of RE-modified Cu-SSZ-13 catalyst.

## 2. Experimental

*2.1 Computational Details*

The initial SSZ-13 model was obtained from the International Zeolite Association database. A CHA structural model with unit cell parameters of 13.6750 × 23.6858 × 14.7670 $Å^3$ was acquired using orthogonalization processing[20]. All First Principles Computational (FPC) and Ab Initio Molecular Dynamics (AIMD) calculations were performed using the CP2K software package[21]. The electronic structure of atoms was

treated with Perdew-Burke-Ernzerhof (PBE) exchange - correlation functional[22], employing a plane-wave cutoff energy of 400 Ry and the DZVP-MOLOPT-SR-GTH basis set as implemented in CP2K. The lnPP2 method was applied for rare earth elements with its distinctive 4f electronic characteristics[23]. Structural optimizations were conducted using the Broyden-Fletcher-Goldfarb-Shanno (BFGS) algorithm, with D3BJ dispersion correction incorporated to accurately describe long-range dispersion interactions[24,25]. Data processing was carried out using the Multiwfn software[26,27], and all structural diagrams were generated with VESTA software[28]. The substitution energy ($E_S$) was calculated according to the following formula:

$$E_S=E_{(RE\text{-}Cu)}-E_{Cu\text{-}SSZ\text{-}13}-\mu_{RE}-\mu_O-\mu_H+\mu_{Cu} \quad (1)$$

Where $E_{(RE\text{-}Cu)}$ represents the total energy of the rare earth-doped system, $E_{(Cu\text{-}SSZ\text{-}13)}$ denotes the energy of the undoped system, and $\mu_{RE}$, $\mu_O$, $\mu_H$, $\mu_{Cu}$, correspond to the chemical potentials of respective chemical elements. A negative $E_S$ value indicates thermodynamic stability, with larger absolute values signifying higher stability.

*2.2 Catalyst preparation*

Rare-Earth modified Cu-SSZ-13 catalysts (RE = La, Ce, Pr, Nd, Sm, Eu, Y) presented in this study were synthesized via a simple impregnation method that is suitable for industrial applications. First, 10 g of Cu-SSZ-13 (Si/Al = 6 ~ 7, Zhengda Energy Environmental Materials (Dalian) Co., Ltd.) was added to 0.1 M $La(NO_3)_3\cdot6H_2O$ (Admas-beta, 99.9%), $Ce(NO_3)_3\cdot6H_2O$ (Admas-beta, 99.99%), $Pr(NO_3)_3\cdot6H_2O$ (Admas-beta, 99.9%), $Nd(NO_3)_3\cdot6H_2O$ (Admas-beta, 99.9%), $Sm(NO_3)_3\cdot6H_2O$ (Admas-beta, 99.9%), $Eu(NO_3)_3\cdot5H_2O$ (Admas-beta, 99.99%) and $Y(NO_3)_3\cdot6H_2O$ (Admas-beta, 99.99%) solutions, respectively. Each mixture was magnetic stirred at 80 ℃ for 2 h, followed by rotary evaporation at 60 ℃ to remove

water and finally calcined in a muffle furnace at 500 ℃ for 2 h to obtain the final catalysts. The as-prepared RE modified Cu-SSZ-13 catalysts were designated as RECuSSZ-13, where RE standed for La, Ce, Pr, Nd, Sm, Eu and Y, respectively. Si/Al ratios, Cu contents and RE loadings of the samples were displayed in Supplementary **Table S1**. The hydrothermal aging treatment of the catalysts was performed in flowing air containing 10 vol.% $H_2O$ at 750 ℃ for 16 h. The resulting catalysts were named as RECuSSZ-13HT.

*2.3 Catalytic performance evaluation*

The $NH_3$-SCR reaction of RECu-F and RECu-HT samples (40 ~ 60 mesh) was conducted in a fixed-bed quartz reactor in the temperature range of 150 ~ 600 ℃. The total flow rate of the reaction gas was set at 750 mL·min$^{-1}$ with a gas hourly space velocity (GHSV) of 100,000 h$^{-1}$. The simulated reaction gas composition included 500 ppm $NH_3$, 500 ppm NO, 10 vol.% $O_2$, and 5 vol.% $H_2O$, with $N_2$ used as the balance gas. The concentrations of outlet gases such as NO, $NO_2$, $N_2O$, and $NH_3$ were analyzed in real-time using a Fourier-transform infrared (FTIR) spectrometer (Antaris IGS, Thermo Scientific, USA). The calculation formulas for $NO_x$ conversion, $N_2$ selectivity, and $N_2O$ concentration are as follows:

$$NO_x \text{ conversion} = \frac{[NO_x]_{inlet} - [NO_x]_{outlet}}{[NO_x]_{inlet}} \times 100\% \quad (2)$$

$$N_2 \text{ selectivity} = \frac{[NO_x]_{inlet} + [NH_3]_{inlet} - [NO_x]_{outlet} - [NH_3]_{outlet} - 2[N_2O]_{outlet}}{[NO_x]_{inlet} + [NH_3]_{inlet} - [NO_x]_{outlet} - [NH_3]_{outlet}} \times 100\% \quad (3)$$

*2.4 Catalyst characterization*

The characterization techniques employed include XRF, ICP, XRD, $H_2$-TPR, $NH_3$-TPD, EPR, XPS, and *in situ* DRIFTS. Detailed information regarding the specific measurement methods can be found in the Supporting Information section.

## 3. Results and discussion

*3.1 Theoretical Screening of Hydrothermal Stability of RECuSSZ-13*

FPC were conducted to screen various RECuSSZ-13 (RE = La, Ce, Pr, Nd, Sm, Eu and Y catalysts and identify promising candidates for $NH_3$-SCR. **Fig. S1** displays the optimized structure models of RECuSSZ-13 according to the reports that $RE^{3+}$ ions are believed to be at 6MRs in the form of $[Z_2RE^{3+}(OH)]^{2+}$ in SSZ-13[12,17,18,29,30]. Initially, we investigate the $E_S$ of different rare earth elements occupying the 6MRs sites in Cu-SSZ-13 to demonstrate whether they can stably present in the 6MRs of Cu-SSZ-13. As illustrated in **Fig. 1a**, the calculated $E_S$ values range from -12 eV to -10 eV, indicating that La, Ce, Pr, Nd, Sm, Eu and Y can replace $Z_2Cu$ in 6MRs of Cu-SSZ-13 to form thermodynamically stable structure of RECuSSZ-13. Subsequently, the Hirshfeld charge[31] analysis (**Fig. 1b**) reveals that the stability order of the $ZCu(OH)^+$ across the systems is as follows: YCuSSZ-13 > SmCuSSZ-13 > CeCuSSZ-13 > EuCuSSZ-13 > NdCuSSZ-13 > Cu-SSZ-13 > PrCuSSZ-13 > LaCuSSZ-13, suggesting significant differences in the influence of RE elements in the 6MRs on the stability of the $ZCu(OH)^+$. Furthermore, the enhancement mechanism of RE cations on the hydrothermal stability of the $ZCu(OH)^+$ species was computed using the CI-NEB method[32] to simulate its transformation into $Cu(OH)_2$, which is a critical step in the conversion of active copper species into inactive CuO, as illustrated in **Fig. 1c** and **1d**. It is evident that the incorporation of rare earth elements affects the reaction energy barrier. Specifically, the transition state energy barriers ($E_{TS}$) follow a descending order of: YCuSSZ-13 (1.71 eV) > NdCuSSZ-13 (1.53 eV) > SmCuSSZ-13 (1.27 eV) > CeCuSSZ-13 (1.23 eV) > EuCuSSZ-13 (1.11 eV) > Cu-SSZ-13 (1.10 eV) > LaCuSSZ-13 (0.89 eV) > PrCuSSZ-13 (0.68 eV), implying that $Cu(OH)_2$ species are more

difficult to form in YCuSSZ-13, NdCuSSZ-13, SmCuSSZ-13, CeCuSSZ-13 and EuCuSSZ-13 samples, thereby improving hydrothermal stability of the SCR reaction.

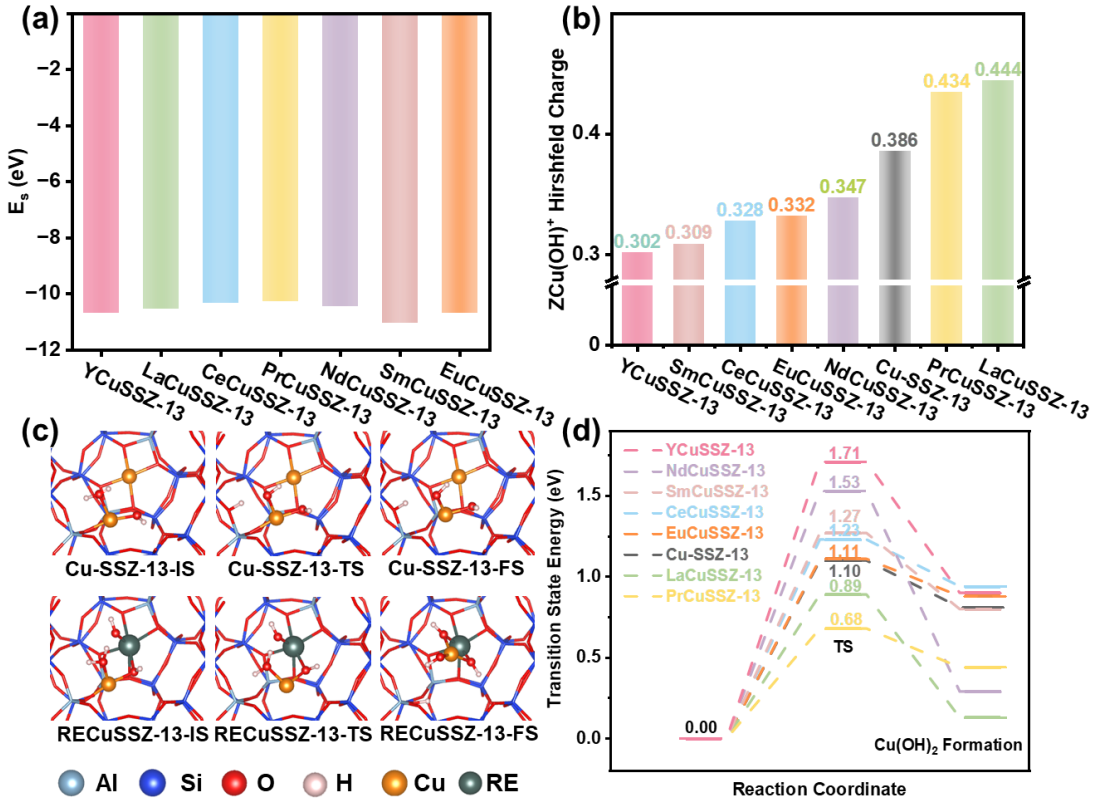



**Fig. 1. Theoretical screening of RE enhancement on hydrothermal stability of RECuSSZ-13.** (a) The substitution energy of RE for $Z_2Cu$ of 6MRs; (b) the Hirshfeld charge distribution for $ZCu(OH)^+$ of 8MRs after RE doping; (c) and (d) the transition state configurations and reaction energy barriers.

*3.2 Catalytic Activity and Hydrothermal Stability*

To validate the predictions of theoretical screening, a series of RECuSSZ-13 (RE = La, Ce, Pr, Nd, Sm, Eu, Y) catalysts were synthesized by a conventional impregnation method. As shown in **Table S1**, all samples are found to contain similar Si/Al ratios (~ 6.2), Cu contents (~ 3.3 wt%) and RE loadings (~ 0.4 wt%). X-ray diffraction (XRD) analysis (**Fig. S2**) reveals that all RECuSSZ-13 samples exhibit a typical CHA framework structure[33], which is in agreement with the theoretical model (**Fig. 1a**). Subsequently, the effect of rare earth species on the catalytic performance of the Cu-

SSZ-13 catalyst in $NH_3$-SCR reactions within the temperature region of 150 ~ 600 ℃ is explored. As shown in **Fig. S3**, most RECuSSZ-13 samples, such as LaCuSSZ-13, CeCuSSZ-13, NdCuSSZ-13, EuCuSSZ-13 and YCuSSZ-13, have negligible improvements in low-temperature catalytic performance compared to Cu-SSZ-13. In contrast, the $NO_x$ conversion of SmCuSSZ-13 at 175 ℃ are nearly 10% higher than that of Cu-SSZ-13 (83%), while the addition of Pr has an inhibitory effect on the activity, which reduces the conversion to 75% at this temperature. In stark contrast to Cu-SSZ-13 (**Fig. 2a, S3** and **S4**), all RECuSSZ-13 catalysts exhibit significantly broadener complete conversion reaction window ($T_{100}$, the temperature at 100% of $NO_x$ conversion), concurrently achieving lower $N_2O$ concentrations as well as superior $N_2$ selectivity.

Normally, the hydrothermal stability of SCR catalysts is an indispensable property for vehicles, which is a key determinant of the catalyst's service life. The denitrification efficiency of the Cu-SSZ-13 catalyst are clearly degraded after the hydrothermal treatment as shown in **Fig. 2b** and other literature reports[17,34-36], but the incorporation of RE prevents the severe loss of $NO_x$ conversion. After hydrothermal ageing at 750 ℃ for 16 h in air containing 10% $H_2O$, the $NO_x$ conversions increase from 26% to 38% for YCuSSZ-13HT and from 28% to 31% for NdCuSSZ-13HT compared with the corresponding fresh counterparts at 150 ℃ (**Fig. S5**), which contrasts sharply with the common reports of deactivation. In spite of the similar low-temperature (< 200 ℃) SCR activity of fresh catalysts, the hydrothermal stability of samples shows great differences (**Fig. 2b** and **2c**). The light-off temperature ($T_{50}$, the temperature at 50% of $NO_x$ conversion) of the hydrothermally aged samples followed an order of YCuSSZ-13HT > NdCuSSZ-13HT > CeCuSSZ-13HT ≈ EuCuSSZ-13HT > SmCuSSZ-13HT > Cu-SSZ-

13HT ≈ LaCuSSZ-13HT ≈ PrCuSSZ-13HT (**Fig. S6**), which is in line with the DFT results. In addition, all RECuSSZ-13HT catalysts show much higher activity in the range of 400 ~ 600 ℃ relative to the reference Cu-SSZ-13HT with a wider catalytic temperature window ($\Delta T_{90}$, $NO_x$ conversion ≥ 90%) (**Fig. S7** and **S8**). Particularly, the $\Delta T_{90}$ of YCuSSZ-13HT and SmCuSSZ-13HT is 175 ~ 555 ℃ and 182 ~ 565 ℃, respectively, which are approximately 100 ℃ broader than 182 ~ 464 ℃ of Cu-SSZ-13HT. From **Fig. 2d**, it is obvious that the $N_2$ selectivity enhancement is still visible, and the $N_2O$ production of all RECuSSZ-13HT catalysts is decreased compared with Cu-SSZ-13HT catalyst.

For SCR catalysts, remarkable low-temperature activity below 200 °C, especially after hydrothermal treatment, is an indispensable characteristic for vehicles because up to 40 ~ 90% of $NO_x$ is emitted during cold start and urban driving conditions[19,37]. Therefore, to systematically investigate the impact of rare-earth element doping on the active copper sites, we excluded rare-earth elements with similar low-temperature activity and selected Y, Nd, Ce, and La as the research subjects. Furthermore, a multidimensional comparative schematic diagram (**Fig. 2e and Table S2**) is systematically constructed to evaluate the comprehensive catalytic performance of YCuSSZ-13HT, NdCuSSZ-13HT, CeCuSSZ-13HT, Cu-SSZ-13HT and LaCuSSZ-13HT catalysts, including their distinct low-temperature activity (175 ℃, $C_{175}$), high-temperature activity (600 ℃, $C_{600}$), the complete conversion reaction window ($\Delta T_{90}$), the average reduction in $NO_x$ conversion before and after hydrothermal aging in the range of 150 ~ 600 ℃ ($\triangle C_{F\text{-}A}$), and the selective temperature window ($\Delta S_{95}$, $N_2$ selectivity ≥ 95%), respectively. Undoubtedly, the YCuSSZ-13HT catalyst exhibits excellent $NH_3$-SCR activity, which is superior to the reported rare earth-modified Cu-

zeolites for the $NH_3$-SCR reaction (**Fig. 2f and Table S3**)[12,17,38-43], highlighting its potential for the application in hydrogen fuel vehicle exhaust aftertreatment systems.

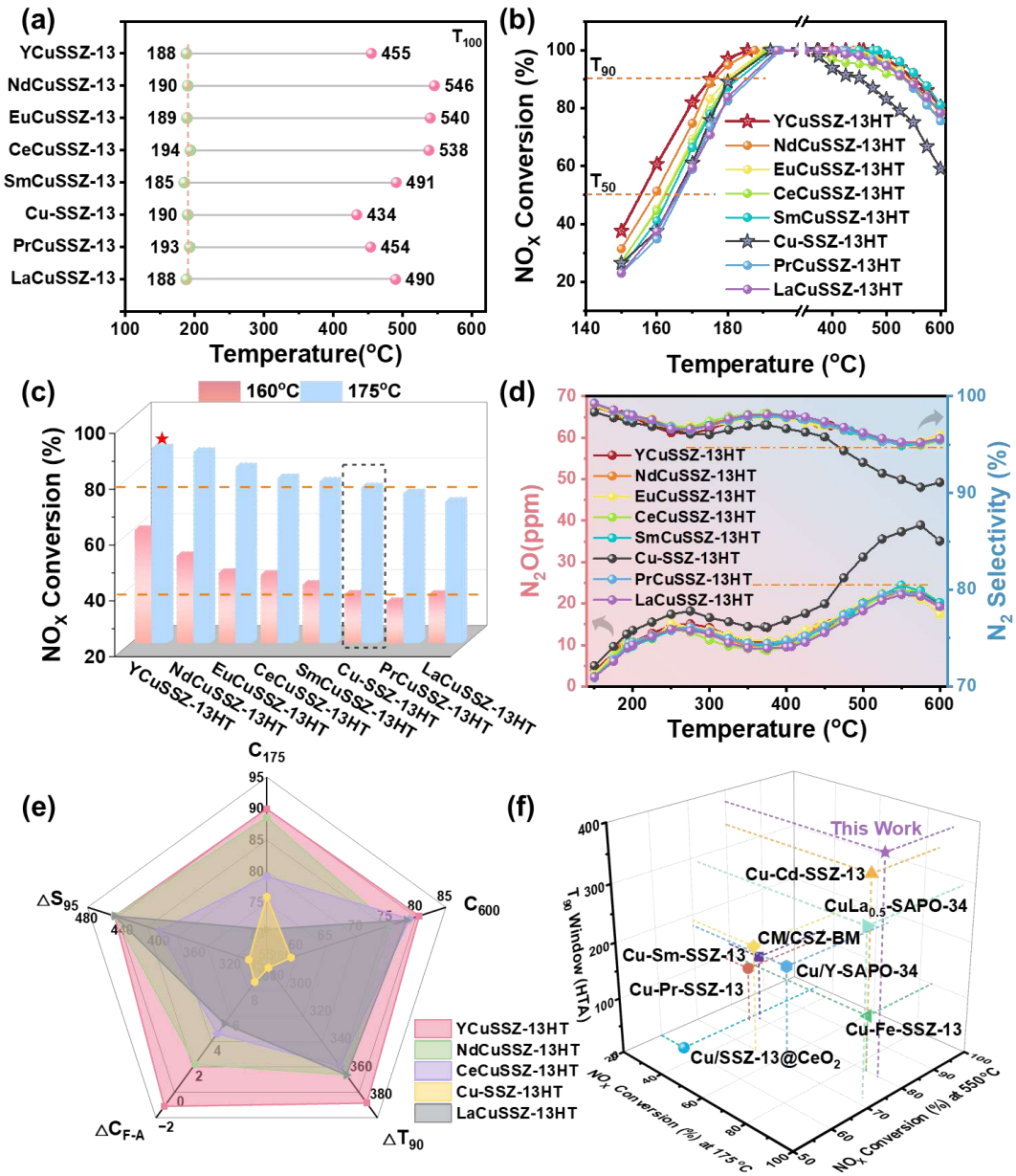



**Fig.2. Catalytic performance of RECuSSZ-13 catalysts.** (a) $T_{100}$ of various fresh catalysts; (b) $NO_x$ conversions *vs.* temperatures of catalysts after hydrothermal ageing at 750 ℃ for 16 h in air containing 10% $H_2O$; (c) plots of $NO_x$ conversions at 160 ℃ and 175 ℃ over hydrothermally aged catalysts; (d) $N_2$ selectivity and $N_2O$ concentrations of hydrothermally aged catalysts; (e) a comparative schematic diagram of hydrothermally aged catalysts; (f) comparison of activity with different reported rare earth modified Cu-zeolites. Reaction conditions: 500 ppm NO, 500 ppm $NH_3$, 10% $O_2$, and 5% $H_2O$, balance $N_2$; GHSV = 100000 $h^{-1}$.

*3.3 Geometry Dynamics of Cu Sites in RECuSSZ-13HT*

To elucidate the effects of doping with different rare earth elements on the catalytic activity of Cu-SSZ-13 sample after hydrothermal aging, a series of characterization techniques, including X-ray photoelectron spectroscopy (XPS), electron paramagnetic resonance (EPR), temperature-programmed desorption of ammonia ($NH_3$-TPD), and diffuse reflectance infrared Fourier transform spectroscopy (DRIFTS) were employed to analyze the coordination environment and distribution of active Cu sites.

The Cu 2*p* of XPS spectra were carried out to investigate active sites of zeolite-confined $Cu^{2+}$ species in Cu-SSZ-13HT and RECuSSZ-13HT catalysts. As shown in **Fig. 3a**, the binding energy (BE) peaks at ~933.1 eV and ~952.8 eV are indicative of Cu $2p_{3/2}$ and Cu $2p_{1/2}$ states, respectively. The shake-up satellite centered at ~944.4 eV is attributed to $Cu^{2+}$ species, confirming the absent of $Cu^{+}$ or $Cu^{0}$ species on all catalysts[41,44]. This finding underscores that the Cu species on Cu-SSZ-13HT and RECuSSZ-13HT catalysts are predominantly present as divalent, indicating that the addition of RE exhibits a minimal effect on the valance states of surface copper. After RE modification, the peaks of Cu $2p_{3/2}$ peaks shift toward to higher BE, indicating that $Cu^{2+}$ has a stronger coordination with the oxygen atoms of the zeolite framework[45]. It is noteworthy that the BE of Cu $2p_{3/2}$ follows an order of LaCuSSZ-13HT (934.0 eV) > CeCuSSZ-13HT (933.7 eV) > NdCuSSZ-13HT (933.4 eV) > YCuSSZ-13HT (933.3 eV) > Cu-SSZ-13HT (933.1 eV). That is, the introduction of Y, Nd, and Ce can enhance the coordination ability between $Cu^{2+}$ species and framework O, thereby improving the stability of the active Cu species and preventing the generation of non-active CuO during the hydrothermal aging process. However, the excessively strong interaction between $Cu^{2+}$ species and framework O in LaCuSSZ-13HT restricts the mobility of Cu ions[46], thereby reducing the low-temperature SCR reactivity. These results agree with our $E_{TS}$ and SCR activity results. After deconvolution, the peak at around 933.1 eV is

ascribed to both tetrahedrally coordinated $Cu^{2+}$ species and CuO nanoparticles, while the peak at ~935.8 eV corresponds to zeolite-confined $Cu^{2+}$ species with octahedral coordination[47,48]. As shown in **Fig. 3b**, the relative contents of $Cu^{2+}$ species in YCuSSZ-13HT (39.3%), NdCuSSZ-13HT (35.7%), CeCuSSZ-13HT (34.2%), and LaCuSSZ-13HT (35.5%) are higher than that in Cu-SSZ-13HT (31.0%). It has been widely accepted that the amount of isolated $Cu^{2+}$ on the surface of catalysts plays an important role in high-temperature SCR activity[45], further validating the superiority of the RE in determining the high-temperature catalytic performance on Cu-SSZ-13 catalysts.

Then, EPR spectra were used to identify more detailed Cu speciation and quantification in the Cu-SSZ-13HT and RECuSSZ-13HT samples due to isolated $Cu^{2+}$ ions ($ZCu(OH)^+$ and $Z_2Cu$) with one unpaired electron having a strong EPR response [49-51]. In contrast, owing to the lack of unpaired electrons and antiferromagnetic effects, $Cu^+$ ions, $CuO_x$ clusters and RE ions are all EPR-silent[52]. **Fig. 3c** presents the essentially identical characteristic values (~3350 G in the high field, $g_{//} = 2.35$, $A_{//} = 152$ G, $g_{\perp} = 2.10$) of all hydrated samples, but the quantity is different (insert in **Fig. 3c**), indicating that the presence of RE induces changes to the local coordination environment of $Cu^{2+}$ and once again proves that the introduction of RE can enable the catalyst to retain more active Cu species after hydrothermal aging. Note that $Z_2Cu$ remains EPR active because of its square planar Cu-O coordination after dehydration, whereas $ZCu(OH)^+$ species becomes silent as a result of the pseudo Jahn-Teller effect[8,50]. As such, $ZCu(OH)^+$ quantification can in principle be straightforward, where EPR areas differences between hydrated and dehydrated catalysts are caused by $ZCu(OH)^+$, as illustrated in **Fig. 3d** and **Table S4**. The normalized $ZCu(OH)^+$ concentration follows the order: YCuSSZ-13HT > NdCuSSZ-13HT > CeCuSSZ-13HT > Cu-SSZ-13HT > LaCuSSZ-13HT, aligning with the order of low-temperature activity.

Specifically, the $ZCu(OH)^+$ concentration in YCuSSZ-13HT increases by 19.3% in comparison with Cu-SSZ-13HT, clearly demonstrating that Y can more effectively preserves isolated $Cu^{2+}$ species after hydrothermal aging, consistent with the XPS results.

Subsequently, $NH_3$-TPD measurements were conducted on the RECuSSZ-13HT catalysts to further quantify the proportion of $ZCu(OH)^+$ and $Z_2Cu$. As already shown in literatures, peaks at ~288 ℃ and ~352 ℃ depicted in **Fig. 3e** after deconvolution analysis could be assigned to $NH_3$ adsorbed on $Z_2Cu$ and $ZCu(OH)^+$ species, respectively[9,53,54]. The ratios of $ZCu(OH)^+$ / ($ZCu(OH)^+$ + $Z_2Cu$) of all the catalysts are shown in **Fig. 3f**. It is noteworthy that $ZCu(OH)^+$ values are 76.4%, 70.9%, 67.5%, 64.5% and 63.2% for YCuSSZ-13HT, NdCuSSZ-13HT, CeCuSSZ-13HT, Cu-SSZ-13HT, and LaCuSSZ-13HT, respectively. This result indicates that the introduced Y, Nd, Ce species increase the total $ZCu(OH)^+$ content, mirroring EPR results, which contributes the distinguished low-temperature activity of YCuSSZ-13HT, NdCuSSZ-13HT, CeCuSSZ-13HT. For LaCuSSZ-13HT, however, the content of $ZCu(OH)^+$ is decreased compared to CuSSZ-13HT. Based on the XPS results, it is speculated that an excessively strong Cu-O interaction in 6MRs hinders the migration of Cu species to 8MRs, which in turn limits the formation of active $ZCu(OH)^+$ species and results in inferior low-temperature activity after hydrothermal aging.

To further explore the influence of RE on the distribution of $Z_2Cu$ and $ZCu(OH)^+$ species within the zeolites, the T-O-T vibration region in the *in situ* DRIFTS spectra recorded after adsorption of $NH_3$ till saturation were performed on various catalysts. As shown in **Fig. S9**, two negative peaks at ~910 $cm^{-1}$ and ~950 $cm^{-1}$ are attributed to the zeolite T-O-T vibrations perturbed by $Z_2Cu$ and $ZCu(OH)^+$, respectively[55-57]. For a more intuitive and clear understanding of the changes in $ZCu(OH)^+$ and $Z_2Cu$ with

introducing RE, peak fittings are used to calculate the area ratios of $ZCu(OH)^+$ and $Z_2Cu$ for all samples (**Fig. 3g**). The concentrations of $ZCu(OH)^+$ in YCuSSZ-13HT (76.2%), NdCuSSZ-13HT (71.5%), and CeCuSSZ-13HT (68.9%) are higher than that in Cu-SSZ-13HT (65.1%), which is in accordance with EPR and $NH_3$-TPD results. This further emphasizes the unusual stability of $ZCu(OH)^+$ in the YCuSSZ-13HT, NdCuSSZ-13HT and CeCuSSZ-13HT catalysts, especially for the YCuSSZ-13HT, reported in this study, as confirmed by FPC.

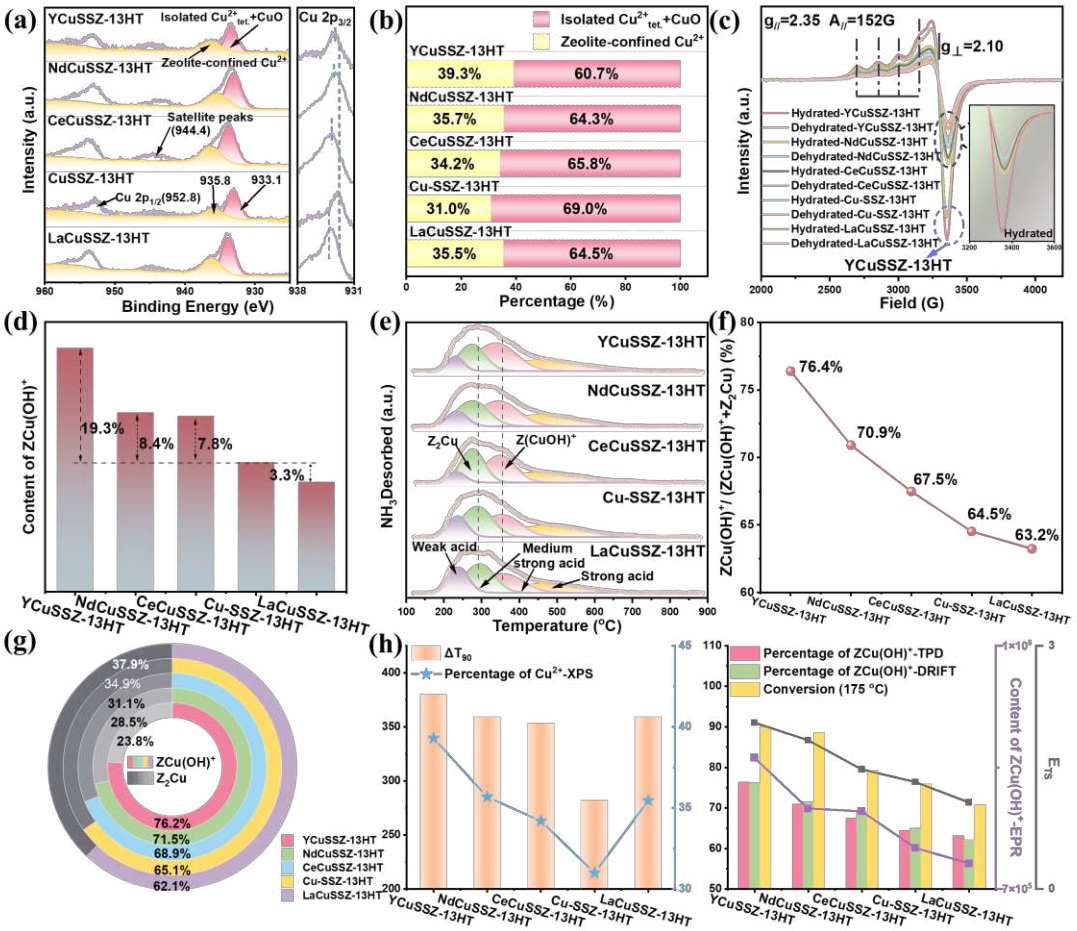



**Fig. 3. Coordination environment and distribution of Cu sites in RECuSSZ-13HT.** (a) Cu 2*p* of XPS spectra; (b) proportion of zeolite-confined $Cu^{2+}$ species as well as isolated $Cu^{2+}$ and CuO nanoparticles; (c) EPR spectra; (d) normalized area of $ZCu(OH)^+$ based on quadratic integration of EPR spectra; (e) $NH_3$-TPD profiles; (f) the percentage of $ZCu(OH)^+$ based on quadratic integration of $NH_3$-TPD spectra; (g) semiquantitative analysis of $NH_3$-DRIFTS; (h) relationship between relative $Cu^{2+}$ and $ZCu(OH)^+$ contents and the SCR performance.

In order to observe the effect of copper species on catalytic activity more intuitively, $\Delta T_{90}$, the $NO_x$ conversion at 175 ℃, $E_{TS}$ against the fraction of isolated $Cu^{2+}$ and $ZCu(OH)^+$ were plotted in **Fig. 3h**. It can be seen that the catalytic temperature window widens along with the fraction of isolated $Cu^{2+}$ increases, and the $NO_x$ conversion at 175 ℃ would undergo a remarkably enhancement when the fraction of $ZCu(OH)^+$ increases. This provides evidence that the introduction of RE has an impact on the coordination environment and distribution of Cu sites, thereby affecting the performance of the catalyst. It is important to note that the strong correlation between $E_{TS}$ and the fraction of $ZCu(OH)^+$ or catalytic performance well suggests that the $E_{TS}$ is a vital factor to determine the hydrothermal stability and it is reliable to utilize it to further forecast the catalytic performance of the RECu-zeolites catalysts after the hydrothermal treatment.

*3.4 Chemical and electronic properties of RECuSSZ-13HT*

Temperature programmed reduction with $H_2$ ($H_2$-TPR) was employed to investigate the effect of RE on reducibility of $Cu^{2+}$ species in RE-modified samples after the hydrothermal treatment. As shown in **Fig.4a**, the $H_2$ consumption trace in the Cu-SSZ-13HT sample can be preliminary divided into three reduction peaks by fitting Gaussian functions, sequentially corresponding to the reduction of $ZCu(OH)^+$ to $Cu^+$ (~ 287.8 ℃), CuO to $Cu^0$ (~ 369.5 ℃), and $Z_2Cu$ to $Cu^+$ (~ 449.1 ℃) [38,44,58]. Similar to Cu-SSZ-13HT, three fitting peaks were also observed for RECuSSZ-13HT samples, indicating that $Cu^{2+}$ exist as $ZCu(OH)^+$, CuO and $Z_2Cu$ species. Note that the $ZCu(OH)^+$ reduction temperature on RECuSSZ-13HT is about 30 ~ 50 ℃ higher than that on Cu-SSZ-13HT, implying that the interaction between $Cu^{2+}$ and zeolite is enhanced after the introduction of RE, and this result is consistent with the XPS characterization. Based on the deconvoluted results (**Fig.4b**), RECu-SSZ-13HT has a higher proportion of isolated $Cu^{2+}$ than Cu-SSZ-13HT, evidencing the higher denitrification efficiency of

the former after the hydrothermal treatment, aligning with the observed catalytic performance. In the case of YCuSSZ-13HT, NdCuSSZ-13HT and CeCuSSZ-13HT, the content of $ZCu(OH)^+$ ions is still higher than that of Cu-SSZ-13HT (**Fig.4b** and **S10**), as corroborated by EPR, $NH_3$-TPD and $NH_3$-DRIFTS results, indicating that the introduction of the proper RE ions (Y, Nd and Ce) maintains the formation of $ZCu(OH)^+$ species and can stabilize $ZCu(OH)^+$, thereby inhibiting the formation of inactive CuO. Specifically, the YCuSSZ-13HT exhibits the most intense reduction peak associated with $ZCu(OH)^+$ species in comparison to the other counterparts, clearly indicating that Y promotes the reduction of $Cu^{2+}$ species. This enhanced reducibility is the primary reason for the superior low-temperature $NH_3$-SCR activity of YCuSSZ-13HT over Cu-SSZ-13HT.

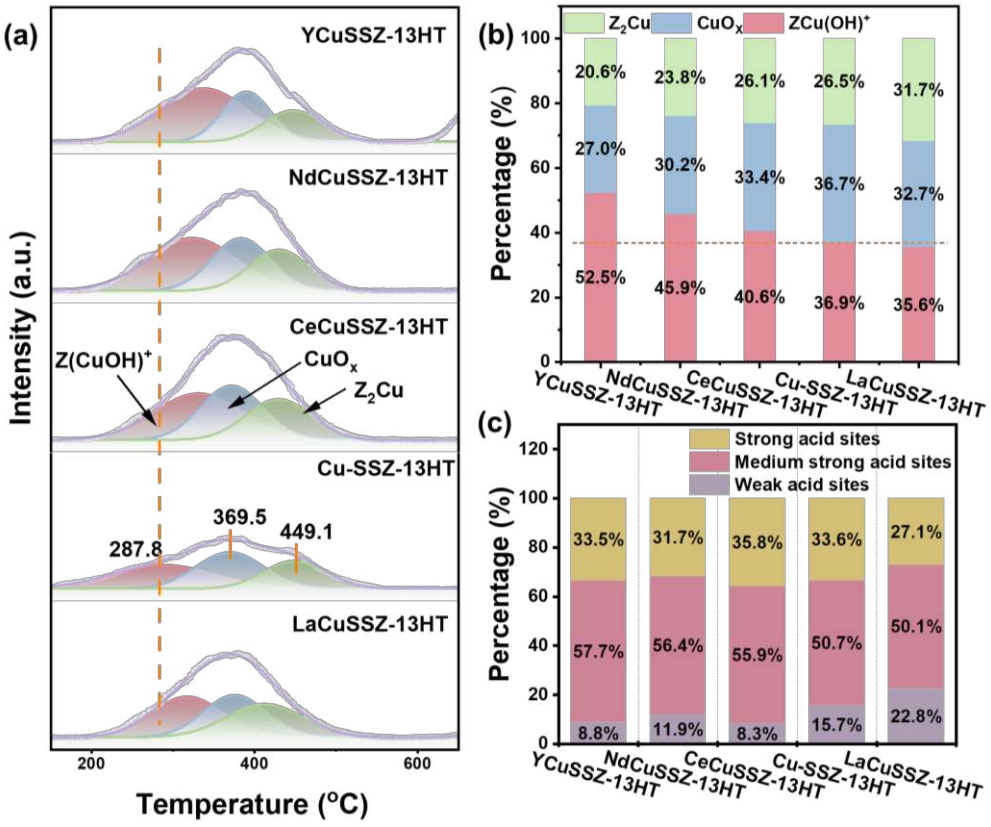



**Fig. 4. Reducibility and acidity of Cu-SSZ-13HT and RECuSSZ-13HT.** (a) $H_2$-TPR profiles; (b) the percentage of different Cu species determined by $H_2$-TPR; (c) the percentage of different acid sites determined by $NH_3$-TPD.

Acidity is an active site for reactive $NH_3$ or acts as a $NH_3$ reservoir for Cu sites, which plays a crucial role towards the overall SCR reaction. Therefore, $NH_3$-TPD measurements were conducted to investigate the $NH_3$ storage capacity on both Lewis-acid and Bronsted-acid sites of all RECuSSZ-13HT catalysts. As shown in **Fig. 3e**, the Cu-SSZ-13HT catalyst exhibits four distinct $NH_3$ desorption peaks centered at 236.6 ℃, 288.3 ℃, 352.1 ℃ and 482.6 ℃, which are sequentially assigned to the desorption of $NH_3$ on weak acid sites specifically extra-framework Al sites, medium-strength Lewis acid sites (L-acid) generated by $Z_2Cu$ and $ZCu(OH)^+$, and strong Brønsted acid sites (B-acid) [40,53,59,60]. By comparing the $NH_3$-TPD profiles, it is evident that the $NH_3$ desorption peaks assigned to $Z_2Cu$ and $ZCu(OH)^+$ of YCuSSZ-13HT, NdCuSSZ-13HT and CeCuSSZ-13HT catalysts shift to lower temperatures compared to those of Cu-SSZ-13HT, while that of LaCuSSZ-13HT shift to higher temperatures. It is argued by Zeng et al.[61] that the downshift of $NH_3$ desorption peaks indicates a weakening in the acid strength of medium-strength acid sites, which is conducive to moderate adsorption and activation of $NH_3$, making it more accessible for interaction with NO, as corroborated by catalytic performance results (**Fig. 2b**). The quantitative $NH_3$ desorption are presented in **Fig. 4c and Table S5**. In comparison to the Cu-SSZ-13HT, YCuSSZ-13HT, NdCuSSZ-13HT and CeCuSSZ-13HT catalysts exhibit lower amount of weak acid sites. This result indicates that the introduced Y, Nd and Ce species could reduce the number of extra-framework Al sites, thereby alleviating the occurrence of dealumination phenomenon during the severe hydrothermal aging process. Moreover, it is observed that the percentage of the medium strong L-acid sites follows an order of YCuSSZ-13HT (57.7 %) > NdCuSSZ-13HT (56.4 %) > CeCuSSZ-13HT (55.9 %) > Cu-SSZ-13HT (50.7%) > LaCuSSZ-13HT (50.1%). As reported[62,63], medium-strength acid sites are the main storage sites for reactive $NH_3$. The abundance of such sites on

YCuSSZ-13HT therefore leads to its superior catalytic performance at low temperatures.

*3.5 Mechanism Studies*

*In situ* DRIFTS at 170 ℃ was selected to probe the reaction intermediates and mechanism of Cu-SSZ-13HT and RECuSSZ-13HT catalysts under various reaction conditions. Initially, the adsorption behavior of NO + $O_2$ was investigated of all samples presaturated with $NH_3$. As shown in **Fig. 5** and **S11-13**, upon $NH_3$ saturation, the adsorption regions centered at 1248, 1615, and 3181 $cm^{-1}$ corresponds to $NH_3$ coordinated with Lewis acid sites (L-acid), while the bands at 1468, 1755, 3269 and 3335 $cm^{-1}$ can be assigned to $NH_4^+$ coordinated with Brønsted acid sites (B-acid)[64-66]. The negative peaks at ~ 3630 $cm^{-1}$ and ~ 3671 $cm^{-1}$ represent the Si-OH and Si-OH-Al structure consumed by the adsorption of $NH_4^+$, respectively [67]. Additionally, the peaks at 2338 and 2358 $cm^{-1}$ are also assigned to $NH_3$ coordinated with L-acid [57]. In striking contrast, this band intensity of the L-acid at 2338 ~ 2358 $cm^{-1}$ for YCuSSZ-13HT is significantly higher than that for NdCuSSZ-13HT, CeCuSSZ-13HT and Cu-SSZ-13HT, and the peak is hardly observed for LaCuSSZ-13HT. This clearly demonstrates that YCuSSZ-13HT possesses the highest acid amount compared to other samples, consistent with the $NH_3$-TPD profiles.

Upon the introduction of NO + $O_2$, a specific amount of $NH_3$ adsorbed on the L-acid and the $NH_4^+$ formed on the B-acid in all samples begin to participate in the reaction and gradually decreased. Regarding the time required for the complete consumption of L-$NH_3$ (~ 1615 $cm^{-1}$), LaCuSSZ-13HT requires approximately 10 min, while the other four samples only need 2 ~ 4 min. The band of B-acid (~ 1468 $cm^{-1}$) disappears at 8 ~10 min over YCuSSZ-13HT, NdCuSSZ-13HT and CeCuSSZ-13HT, while the corresponding band on the Cu-SSZ-13HT and LaCuSSZ-13HT disappears at

15 min. These results confirm that the Y, Nd and Ce modification promoted both L-$NH_3$ and B-$NH_4^+$ to participate in the $NH_3$-SCR, which is align with the high catalytic activity at a low temperature. As the introduction time of NO + $O_2$ going on, some new bands derived from the bidentate nitrate species (~1570 $cm^{-1}$ and ~1598 $cm^{-1}$)[68], monodentate nitrates (~1507 $cm^{-1}$)[16,69], $NO^+$ (~1451 $cm^{-1}$)[16] and ionic nitrate species (~1330 $cm^{-1}$)[38] appeared on YCuSSZ-13HT, NdCuSSZ-13HT, CeCuSSZ-13HT and Cu-SSZ-13HT catalysts. In contrast, only bidentate nitrate and monodentate nitrate species are observed on LaCuSSZ-13HT, indicating that the addition of La inhibits the adsorption of NO, which is in line with its poor activity. **Fig. 5e, 5f** and **Table S6** display the comparison of the occurrence and disappearance of various types of nitrate species on RECuSSZ-13HT and Cu-SSZ-13HT catalysts. It is important to note that the production time of ionic nitrate species on YCuSSZ-13HT and NdCuSSZ-13HT (25 min) are much earlier than that on Cu-SSZ-13HT (40 min) (**Fig. 5e**). Moreover, the monodentate nitrates are observed on the YCuSSZ-13HT after initial 2 min exposure and disappears at 20 min, whereas this specie appears relatively late on other catalysts and remain almost constant over 40 min (**Fig. 5f**). These results indicate that YCuSSZ-13HT is more favorable for the adsorption and activation of $NO_x$ intermediates, contributing to its superior catalytic performance. Rather curiously, as displayed in **Fig. S14**, peaks intensity in the range of 3500 ~ 3000 $cm^{-1}$ increases slightly with introducing the NO + $O_2$ and reaches their maximum values at 10 min (YCuSSZ-13HT and NdCuSSZ-13HT), 15 min (CeCuSSZ-13HT and Cu-SSZ-13HT) and 30 min (LaCuSSZ-13HT), respectively. Subsequently, these peaks decrease at different rates, among which the decrease rate in YCuSSZ-13HT is the fastest. Since the 3500 ~ 3000 $cm^{-1}$ bands are not related to nitrates, we propose that the increase in intensity of these peaks upon NO admission can be explained as the formation of $NH_4^+$ intermediates

resulting from the interaction of NO and $NH_3$ ($-NH_3 + NO \rightarrow -NH_2NO + H^+$, $H^+ + NH_3 \rightleftharpoons NH_4^+$), as proved by Chen et al.[70] and Zhang et al.[57]. This unequivocally demonstrates the superior reaction rate-enhancing capability of YCuSSZ-13HT, which agrees well with the SCR performance.

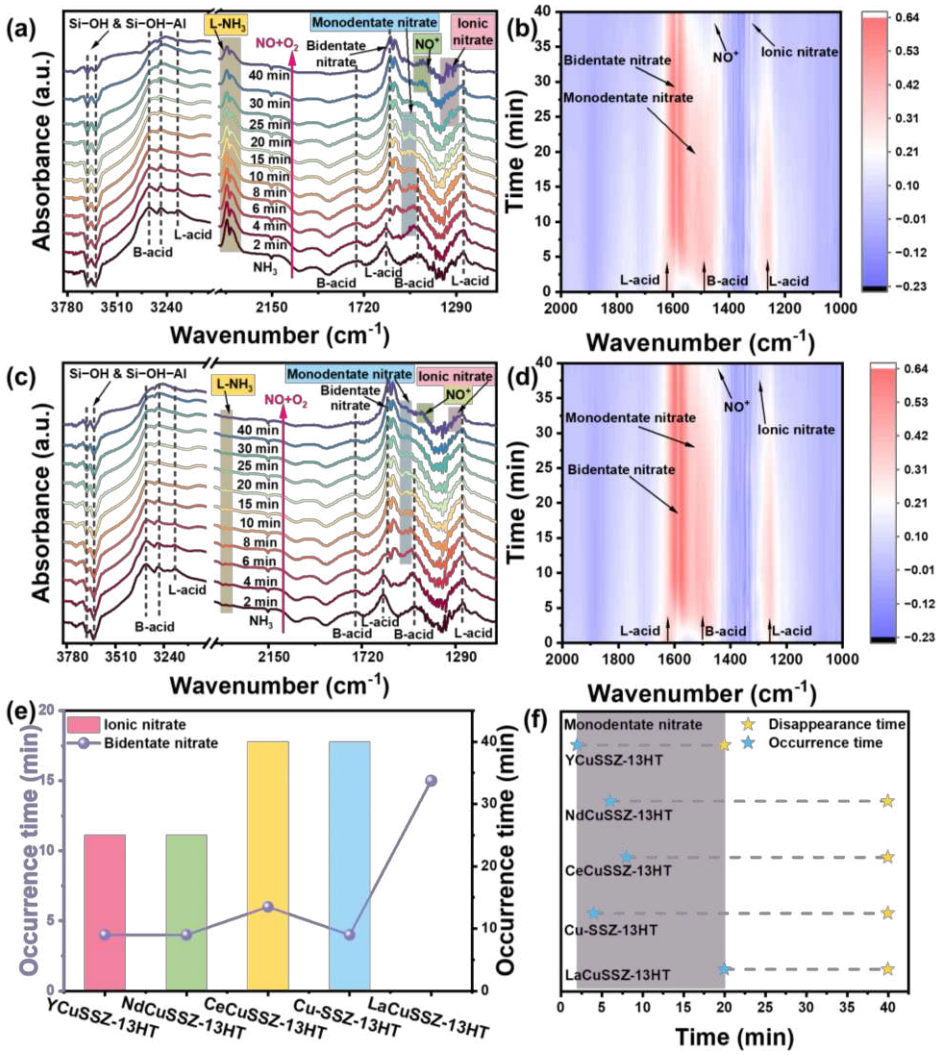



**Fig. 5. Time-dependent *in situ* DRIFTS of transient reactions between NO + $O_2$ and pre-adsorbed $NH_3$ at 170 °C**. (a, b) YCuSSZ-13HT; (c, d) Cu-SSZ-13HT; (e) comparative analysis of the occurrence time of bidentate nitrate and nitrate species over RECuSSZ-13HT and Cu-SSZ-13HT catalysts; (f) temporal comparison of the occurrence and disappearance of monodentate nitrate species over RECuSSZ-13HT and Cu-SSZ-13HT catalysts.

Afterwards, **Fig. S15-19** compare the *in situ* DRIFT spectra of the transient reaction between $NH_3$ and pre-adsorbed NO + $O_2$ on Cu-SSZ-13HT and RECuSSZ-

13HT samples. It can be seen that bidentate nitrates (~1573 and ~1600 $cm^{-1}$) and adsorbed nitrate (~1620 $cm^{-1}$) [71] are observed for all catalysts. After switching to $NH_3$, the bands of these nitrate compounds on the YCuSSZ-13HT rapidly disappear within 4 min, while on the other samples they vanish immediately within 2 min, indicating that the existence of Y promotes the formation of more various nitrates on the catalyst surface. As consistently demonstrated by FPC, EPR, $H_2$-TPR, and $NH_3$-TPD analyses, the YCuSSZ-13HT catalyst has the highest concentration of $ZCu(OH)^+$ groups. Since $ZCu(OH)^+$ species are reported to deliver superior redox capability compared to $Z_2Cu$ species[17,19], this abundance consequently promotes the formation of more adsorbed nitrate species on YCuSSZ-13HT. Concurrently, $NH_3$ coordinated with L-acid and $NH_4^+$ coordinated with B-acid emerge and accumulate on all catalyst surface. Besides, as the reaction progresses, bridging nitrates[72] around at ~1635 $cm^{-1}$ are observed on YCuSSZ-13HT, NdCuSSZ-13HT and CeCuSSZ-13HT. These results above indicate that all types of $NO_x$ adsorbed can participate in the SCR reaction, and the formation of bridging nitrates considered as an intermediate species can be decomposed into $N_2$ and $H_2O$, thus leading to the significant SCR activity. Collectively, *in situ* DRIFTS analysis of the transient reactions revealing that the adsorbed $NH_3^*$ or $NH_4^+$ species can simultaneously react with gaseous NO and adsorbed nitrate species. It is reasonable to believe that Cu-SSZ-13HT and RECuSSZ-13HT follow a mixed reaction pathway involving both Eley-Rideal (E-R) and Langmuir-Hinshelwood (L-H) mechanisms [73,74]. Compared with Cu-SSZ-13HT and LaCuSSZ-13HT, however, the YCuSSZ-13HT, NdCuSSZ-13HT and CeCuSSZ-13HT exhibits better adsorption and activation of NO and $NH_3$ specie, which leads to superior low-temperature activity after hydrothermal.

*3.6 Intrinsic Insight into Enhancement of Hydrothermal Stability*

Finally, we performed Crystal Orbital Hamilton Population (COHP) calculations to better understand the influence of RE elements on the deactivation mechanism of

$ZCu(OH)^+$[75,76]. The analysis focused on the chemical bond strength between $ZCu(OH)^+$ and the zeolite framework, as illustrated in **Fig. 6a**. The projected COHP (pCOHP) and Integrated COHP (ICOHP) results for the Cu-SSZ-13 and RECuSSZ-13 (RE = Y, Nd, Ce, La) structures are presented in **Fig. 6b, 6c** and **Fig. S20**, respectively. These results indicate that the binding strength between $ZCu(OH)^+$ and the zeolite framework in YCuSSZ-13 (-34.4798 eV) is higher than that in the Cu-SSZ-13 structure (-33.6011 eV), demonstrating that Y doping enhances the interaction between the zeolite framework and $ZCu(OH)^+$. Besides, compared to Cu-SSZ-13, Nd (-34.3957 eV) and Ce (-33.8268 eV) doping also strengthen the chemical bonding, whereas La (-33.3460 eV) doping weakens it. The stronger binding energy increases the difficulty for $ZCu(OH)^+$ to desorb from the zeolite framework, thereby raising the energy barrier for deactivation and contributing to the improved anti-deactivation performance of the YCuSSZ-13, NdCuSSZ-13 and CeCuSSZ-13 in the hydrothermal aging process. This observation aligns with the FPC and catalytic activity trends exhibited in **Fig. 1 and Fig. 2**.

To elucidate the effect of bond strength variation on the removal behavior of $ZCu(OH)^+$, AIMD simulations were conducted at 750 ℃ for 10 ps. The temporal evolution of potential energy is shown in **Fig. 6d**, with the points indicating the formation of $Cu(OH)_2$, and deactivation structures of Cu-SSZ-13 and RECuSSZ-13 (RE = Y, Nd, Ce, La) are displayed in **Fig. 6e, 6f**, and **Fig. S21-23,** respectively. The results indicate that doping with rare earth elements significantly alters the deactivation time of $ZCu(OH)^+$. The effectiveness of rare earth modification follows the order: YCuSSZ-13 > NdCuSSZ-13 > CeCuSSZ-13 > Cu-SSZ-13 > LaCuSSZ-13, implying that La doping facilitates deactivation, whereas Ce, Nd, and Y doping delay the process. Among them, the YCuSSZ-13 structure exhibits the longest deactivation time, indicating that Y doping most significantly enhances the stability of $ZCu(OH)^+$.

Combined with Hirshfeld charge distribution and $E_{TS}$ analyses presented in **Fig. 1**, it is evident that RE elements doping in 6MRs induces charge redistribution of $ZCu(OH)^+$ in 8MRs, thereby affecting its binding strength with the zeolite framework. This phenomenon further affects the transition state energy barrier for the formation of $Cu(OH)_2$ from $ZCu(OH)^+$, modulating the difficulty of the removal reaction, and ultimately exerting a substantial impact on its hydrothermal stability. Therefore, by combining the analysis of computational and experimental results, it ban be proved that the introduction of Y, Nd and Ce, especially Y, within the 6MRs effectively promotes the active and stability of $ZCu(OH)^+$ species, leading to the superior low-temperature $NH_3$-SCR performance after hydrothermal ageing.

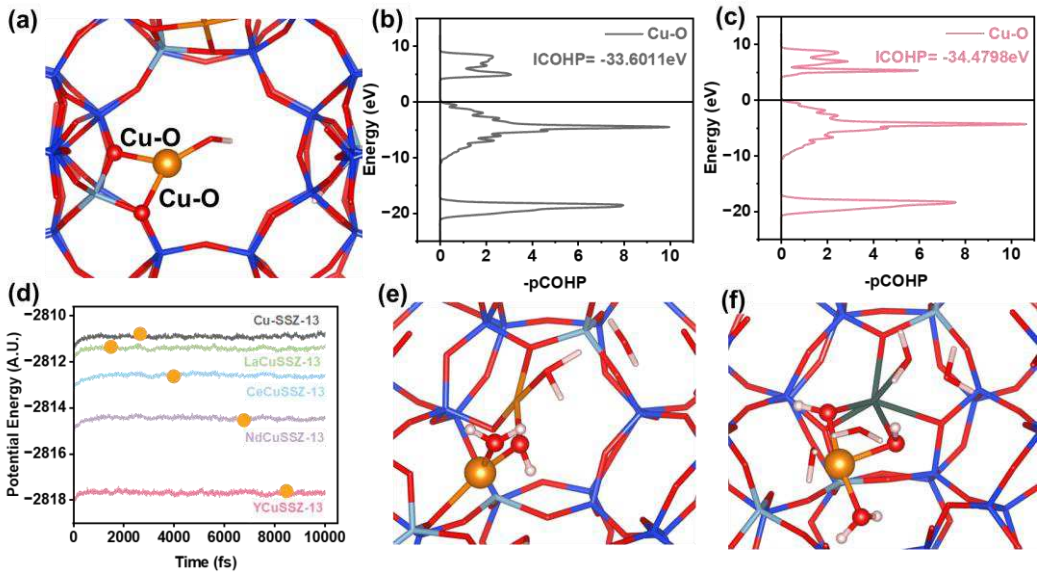



**Fig. 6. COHP and AIMD calculations results.** (a) The bonding configuration between $ZCu(OH)^+$ and the zeolite framework; (b-c) COHP analysis results of the Z-Cu bonds in the Cu-SSZ-13 (Cu-F) and YCuSSZ-13 structures, respectively; (d) energy variation diagram from AIMD simulations for Cu-SSZ-13, LaCuSSZ-13, CeCuSSZ-13, NdCuSSZ-13, and YCuSSZ-13 structures; (e-f) the structural schematics at the moment of deactivation during AIMD simulations for Cu-SSZ-13 and YCuSSZ-13, wherein the orange, red, and white spheres represent the copper, oxygen, and hydrogen atoms, respectively.

## 4. Conclusion

RE-modified Cu-SSZ-13 catalyst holds significant promise for $NO_x$ abatement in actual applications of emission aftertreatment system. However, systematic investigations on the structure-activity relationships of different RE elements in hydrothermally aged Cu-SSZ-13 catalysts remains highly uncertain. In this work, a combined computational and experimental approaches is performed to screen 7 lanthanide RE-modified Cu-SSZ-13, and results indicate that all RE ions can stably present in the 6MRs of Cu-SSZ-13, but their efficacy in stabilizing the $ZCu(OH)^+$ species varies significantly with the specific RE element. An YCuSSZ-13 sample with optimal reducibility and surface acidity has been screened out and exhibits catalytic temperature window of ~100 ℃ wider than that of conventional Cu-SSZ-13 after hydrothermal ageing. Transient reactions reveal that the interaction between Y and Cu species in YCuSSZ-13HT not only significantly enhanced the reaction rate of L-$NH_3$ and B-$NH_4^+$ involved in the $NH_3$-SCR, but also is more favorable for the adsorption and activation of $NO_x$ intermediates. Further COHP and AIMD calculations show that doping Y element in 6MRs more effectively induces charge redistribution of $ZCu(OH)^+$ in 8MRs, increases the transition state energy barrier for the formation of $Cu(OH)_2$ from $ZCu(OH)^+$, modulates the difficulty of the removal reaction, and ultimately has a significant impact on its low-temperature activity after hydrothermal aging. Overall, this study not only confirms the feasibility of theoretical predictions in guiding experimental outcomes but also provides a robust theoretical foundation for the design of zeolite catalysts with superior low-temperature activity after hydrothermal aging.

## Author contributions

L. Y., Y. W. and P. X. conceptualized and designed the DFT calculations and experiments. L. Y. conducted the experimental work, while Y. W. performed the DFT calculations respectively. T. Z., H. Q., X. G., C. Z., and M. Y. provided essential characterization resources and contributed to the interpretation of the data. Y. W. and P. X. supervised the project and took primary responsibility for polishing the manuscript. All authors offered valuable feedback and contributed to the research direction, data analysis, and finalization of the manuscript.

## Declaration of competing interest

The authors declare that they have no known competing financial interests or personal relationships that could have appeared to influence the work reported in this paper.

## Data availability statement

All data supporting the findings of this study are available within the paper and its Supplementary Information.

## Acknowledgements

This work was financially supported by the Advanced Materials-National Science and Technology Major Project (2024ZD0606500), National Natural Science Foundation of China (22278365), Natural Science Foundation of Inner Mongolia Autonomous Region of China (2024MS02008 and 2025QN02048), and the Independent Project of Baotou Research Institute of Rare Earths (2025Z2632).

## References

[1] Koike M*, et al.* Cold-start performance of an ammonia-fueled spark ignition engine with an on-board fuel reformer. *Int. J. Hydrogen Energy.* **46**, 25689-25698 (2021).
[2] Qi YL*, et al.* A review on ammonia-hydrogen fueled internal combustion engines. *eTransportation* **18**, 100288 (2023).
[3] Barth S*, et al.* Tailoring the active sites in Cu-SSZ-13 as a catalyst for the selective catalytic reduction of $NH_3$ to minimize HCHO and HCN emissions. *Nat. Catal.* **8**,

804-821 (2025).
[4] Shan YL, *et al.* Strikingly distinctive $NH_3$-SCR behavior over Cu-SSZ-13 in the presence of $NO_2$. *Nat Commun.* **13**, 4606 (2022).
[5] Krishna SH, *et al.* Influence of framework Al density in Chabazite zeolites on copper ion mobility and reactivity during $NO_x$ selective catalytic reduction with $NH_3$. *Nat. Catal.* **6**, 276-285 (2023).
[6] Singh S, *et al.* Inhibition of $NH_3$-SCR over Cu-CHA at high partial pressures of water: Measurements and DFT-based kinetic modeling. *J. Catal.* **446**, 116071 (2025).
[7] Kim Y, *et al.* Improvement of low-temperature $NO_x$ reduction performance of $NH_3$-SCR with $O_3$ injection under diesel engine transient conditions. *Fuel* **392**, 134817 (2025).
[8] Wang ZH, *et al.* Manganese migration to regulate copper sites in Cu-SSZ-13 for enhanced low-temperature SCR of $NO_x$. *Appl. Catal. B Environ.* **367**, 125107 (2025).
[9] Villamaina R, *et al.* Speciation of Cu cations in Cu-CHA catalysts for $NH_3$-SCR: effects of $SiO_2/AlO_3$ ratio and Cu-loading investigated by transient response methods. *ACS Catal.* **9**, 8916-8927 (2019).
[10] Liu GQ, *et al.* Selective catalytic reduction of $NO_x$ with $NH_3$ over copper-based catalysts: recent advances and future prospects. *EES Catal.* **2**, 231-252 (2024).
[11] Chen ZQ, *et al.* Controllable positions of $Cu^{2+}$ to enhance low-temperature SCR activity on novel Cu-Ce-La-SSZ-13 by a simple one-pot method. *Chem. Commun.* **56**, 2360-2363 (2020).
[12] Chen MY, *et al.* Improving the hydrothermal stability of Al-rich Cu-SSZ-13 zeolite via Pr-ion modification. *Chem. Sci.* **15**, 5548-5554 (2024).
[13] Zhang YN, *et al.* Probing active-site relocation in Cu/SSZ-13 SCR catalysts during hydrothermal aging by in situ EPR spectroscopy, kinetics studies, and DFT calculations. *ACS Catal.* **10**, 9410-9419 (2020).
[14] Lee H, *et al.* Control of the Cu ion species in Cu-SSZ-13 via the introduction of $Co^{2+}$ Co-cations to improve the $NH_3$-SCR activity. *Catalysis Science & Technology* **11**, 4838-4848 (2021).
[15] Wang JG, *et al.* The promotion effect of Niobium on the low-temperature activity of Al-rich Cu-SSZ-13 for selective catalytic reduction of $NO_x$ with $NH_3$. *Chem. Eng. J.* **418**, 129433 (2021).
[16] Kang N, *et al.* Understanding enhancement of strong copper-Yttrium interactions on catalytic properties of Cu/Y-SSZ-13 for $NH_3$-SCR. *Chem. Eng. J.* **475**, 146114 (2023).
[17] Chen MY, *et al.* Unveiling secondary-ion-promoted catalytic properties of Cu-SSZ-13 zeolites for selective catalytic reduction of $NO_x$. *J. Am. Chem. Soc.* **144**, 12816-12824 (2022).
[18] Chen MY, *et al.* La ions-enhanced $NH_3$-SCR performance over Cu-SSZ-13 catalysts. *Nano Res.* **16**, 12126-12133 (2023).
[19] Wang Y, *et al.* Manipulating internal catalytic microenvironment of dynamic Cu/SSZ-13 catalysts by in situ Ce incorporation for efficient $NH_3$-SCR. *J. Environ.*

*Chem. Eng.* **13**, 118403 (2025).
[20] Baerlocher C ML. Database of Zeolite Structures: http://www.iza-structure.org/databases/.).
[21] Kühne TD*, et al.* CP2K: An electronic structure and molecular dynamics software package - Quickstep: Efficient and accurate electronic structure calculations. *J. Chem. Phys.* **152**, 194103 (2020).
[22] Perdew JP*, et al.* Generalized gradient approximation made simple. *Phys. Rev. Lett.* **77**, 3865-3868 (1996).
[23] Lu JB*, et al.* Norm-Conserving 4f-in-Core pseudopotentials and basis sets optimized for trivalent Lanthanides (Ln = Ce–Lu). *J. Chem. Theory. Comput.* **19**, 82-96 (2023).
[24] Grimme S*, et al.* Effect of the damping function in dispersion corrected density functional theory. *J. Comput. Chem.* **32**, 1456-1465 (2011).
[25] Grimme S*, et al.* A consistent and accurate ab initio parametrization of density functional dispersion correction (DFT-D) for the 94 elements H-Pu. *J. Chem. Phys.* **132**, 154104 (2010).
[26] Lu T, Chen FW. Multiwfn: A multifunctional wavefunction analyzer. *J. Comput. Chem.* **33**, 580-592 (2012).
[27] Lu T. A comprehensive electron wavefunction analysis toolbox for chemists, Multiwfn. *J. Chem. Phys.* **161**, 082503 (2024).
[28] Momma K, Izumi F. VESTA 3 for three-dimensional visualization of crystal, volumetric and morphology data. *J. Appl. Crystallogr.* **44**, 1272-1276 (2011).
[29] Kang N*, et al.* Understanding enhancement of strong copper-Yttrium interactions on catalytic properties of Cu/Y-SSZ-13 for $NH_3$-SCR. *Chem. Eng. J.* **475**, 146114 (2023).
[30] Kang N*, et al.* Insights into the enhancement of copper-Lanthanum interactions on the potassium tolerance of Cu/La-SSZ-13 for $NH_3$-SCR. *Chem. Eng. J.* **516**, 164041 (2025).
[31] Hirshfeld FL. Bonded-atom fragments for describing molecular charge densities. *Theor. Chim. Acta.* **44**, 129-138 (1977).
[32] Henkelman G*, et al.* A climbing image nudged elastic band method for finding saddle points and minimum energy paths. *J. Chem. Phys.* **113**, 9901-9904 (2000).
[33] Ma Y*, et al.* Improved hydrothermal durability of Cu-SSZ-13 $NH_3$-SCR catalyst by surface Al modification: Affinity and passivation. *J. Catal.* **405**, 199-211 (2022).
[34] Xu SH*, et al.* Engineering $CeZrO_x$-Cu/SSZ-13 coupled catalysts to synergistically enhance the low-temperature $NH_3$-SCR activity. *Chem. Eng. J.* **476**, 146767 (2023).
[35] Lu S*, et al.* Ultra-high hydrothermal stability of Ce-based $NH_3$-SCR catalyst for diesel engines: A substitute for Cu zeolites. *Fuel* **338**, 127263 (2023).
[36] Liu ZQ*, et al.* Understanding the hydrothermal stability of potential $NH_3$-SCR catalyst Cu-KFI zeolite. *ACS Catal.* **14**, 1678-1689 (2024).
[37] Han JF*, et al.* Cu-OFF/ERI zeolite: Intergrowth structure synergistically boosting selective catalytic reduction of $NO_x$ with $NH_3$. *J. Am. Chem. Soc.* **146**, 7605-7615 (2024).

[38] Li M, *et al.* The preferential occupying effect regulated atomically dispersed Cu site over Cu-SSZ-13 for enhancing $NH_3$-SCR performance. *Fuel* **380**, 133202 (2025).
[39] Zhang JN, *et al.* Enhancing hydrothermal stability in Cu/SSZ-13 catalyst for diesel SCR applications through a novel core-shell structure. *Chin. Chem. Lett.* **36**, 110516 (2025).
[40] Li GB, *et al.* One stone four birds: The redox and acid-basic site integral regulation by La in Cu-SAPO-34 for boosting NO reduction. *Appl. Catal. B Environ.* **378**, 125647 (2025).
[41] Gao LY, *et al.* Boosting low-temperature and high-temperature hydrothermal stability of Cu/SAPO-34 for NO removal via Yttrium decoration. *Chem. Eng. J.* **455**, 140520 (2023).
[42] Andana T, *et al.* Selective catalytic reduction of $NO_x$ with $NH_3$ over Ce-Mn oxide and Cu-SSZ-13 composite catalysts – low temperature enhancement. *Appl. Catal. B Environ.* **316**, 121522 (2022).
[43] Tan MJ, *et al.* Introduction of iron by a feasible way to regulate Cu sites of Cu-SSZ-13 with enhanced hydrothermal stability and $SO_2$ resistance for $NH_3$-SCR. *Micropor Mesopor Mat.* **394**, 113668 (2025).
[44] Jia LF, *et al.* Interface engineering of a bifunctional Cu-SSZ-13@CZO core–Shell catalyst for boosting potassium ion and $SO_2$ tolerance. *ACS Catal.* **12**, 11281-11293 (2022).
[45] Wang JG, *et al.* Unique responses of Cu-SSZ-13 toward phosphorus: Al atoms on zeolite framework versus varied Cu species. *Chem. Eng. J.* **455**, 140379 (2023).
[46] Lee H, *et al.* Mobility of Cu ions in Cu-SSZ-13 determines the reactivity of selective catalytic reduction of $NO_x$ with $NH_3$. *J. Phys. Chem. Lett.* **12**, 3210-3216 (2021).
[47] Artiglia L, *et al.* In situ X-ray photoelectron spectroscopy detects multiple active sites involved in the selective anaerobic oxidation of methane in copper-exchanged zeolites. *ACS Catal.* **9**, 6728-6737 (2019).
[48] Lv H, *et al.* Plasma-catalytic direct oxidation of methane to methanol over Cu-MOR: Revealing the zeolite-confined $Cu^{2+}$ active Sites. *Chem. Eng. J.* **496**, 154337 (2024).
[49] Wu YQ, *et al.* Insights into palladium poisoning of Cu/SSZ-13 selective catalytic reduction catalysts. *Appl. Catal. B Environ.* **331**, 122673 (2023).
[50] Song J, *et al.* Toward rational design of Cu/SSZ-13 selective catalytic reduction catalysts: Implications from atomic-level understanding of hydrothermal stability. *ACS Catal.* **7**, 8214-8227 (2017).
[51] Wu YQ, *et al.* Rate controlling in low-temperature standard $NH_3$-SCR: implications from operando EPR spectroscopy and reaction kinetics. *J. Am. Chem. Soc.* **144**, 9734-9746 (2022).
[52] Chen ZQ, *et al.* Migration of cations and shell functionalization for Cu-Ce-La/SSZ-13@ZSM-5: The contribution to activity and hydrothermal stability in the selective catalytic reduction reaction. *J. Catal.* **392**, 217-230 (2020).
[53] An Q, *et al.* Designing a bifunctional Pt/Cu-SSZ-13 catalyst for ammonia-selective

catalytic oxidation with superior selectivity. *ACS Catal.* **13**, 6851-6861 (2023).
[54] Daya R, *et al.* Kinetics and thermodynamics of ammonia solvation on $Z_2Cu$, ZCuOH and ZCu sites in Cu-SSZ-13 – implications for hydrothermal aging. *Appl. Catal. B Environ.* **297**, 120444 (2021).
[55] Zhang ST, *et al.* Efficient regeneration of Cu-SSZ-13 $NH_3$-SCR catalysts deactivated by Na, P and (Na+P) poisoning. *Chem. Eng. J.* **506**, 160054 (2025).
[56] Wang A, Olsson L. Insight into the $SO_2$ poisoning mechanism for $NO_x$ removal by $NH_3$-SCR over Cu/LTA and Cu/SSZ-13. *Chem. Eng. J.* **395**, 125048 (2020).
[57] Zhang YN, *et al.* Using transient FTIR spectroscopy to probe active sites and reaction intermediates for selective catalytic reduction of NO on Cu/SSZ-13 catalysts. *ACS Catal.* **9**, 6137-6145 (2019).
[58] Shan YL, *et al.* Hydrothermal aging alleviates the inhibition effects of $NO_2$ on Cu-SSZ-13 for $NH_3$-SCR. *Appl. Catal. B Environ.* **275**, 119105 (2020).
[59] Song KL, *et al.* Zinc and phosphorus poisoning tolerance of Cu-SSZ-13 and Ce-Cu-SSZ-13 in the catalytic reduction of nitrogen oxides. *J. Colloid Interface Sci.* **629**, 243-255 (2023).
[60] Gao F, *et al.* Effects of alkali and alkaline earth cocations on the activity and hydrothermal stability of Cu/SSZ-13 $NH_3$–SCR catalysts. *ACS Catal.* **5**, 6780-6791 (2015).
[61] Zeng PX, *et al.* Low temperature SCR denitration with $NH_3$ via synergistic effect of highly dispersed Fe-Co sites. *Chem. Eng. J.* **504**, 159044 (2025).
[62] Zhu N, *et al.* Understanding Na functions on distribution of Cu species within Cu-SSZ-13 for the selective reduction of NO with $NH_3$. *Sep. Purif. Technol.* **347**, 127630 (2024).
[63] Xie MJ, *et al.* Mechanistic insights into the cobalt promotion on low-temperature $NH_3$-SCR reactivity of Cu/SSZ-13. *Sep. Purif. Technol.* **315**, 123617 (2023).
[64] Jiang BQ, *et al.* Plasma-enhanced low temperature $NH_3$-SCR of $NO_x$ over a Cu-Mn/SAPO-34 catalyst under Oxygen-rich conditions. *Appl. Catal. B Environ.* **286**, 119886 (2021).
[65] Jia LF, *et al.* Interface induced by hydrothermal aging boosts the low-temperature activity of Cu-SSZ-13 for selective catalytic reduction of $NO_x$. *Environ. Sci. Technol.* **58**, 15038-15051 (2024).
[66] Shen YL, *et al.* Revealing the mechanism of K-enhanced Cu-SSZ-13 catalysts against hydrothermal aging and P-poisoning for $NO_x$ reduction by $NH_3$-SCR. *Sep. Purif. Technol.* **330**, 125248 (2024).
[67] Su WK, *et al.* Reaction pathway investigation on the selective catalytic reduction of NO with $NH_3$ over Cu/SSZ-13 at low temperatures. *Environ. Sci. Technol.* **49**, 467-473 (2014).
[68] Jiang H, *et al.* Effect of sulfur poisoning on the performance and active sites of Cu/SSZ-13 catalyst. *Chem. Eng. Sci.* **226**, 115855 (2020).
[69] Luo N, *et al.* Hierarchical structured Ti-doped $CeO_2$ stabilized $CoMn_2O_4$ for enhancing the low-temperature $NH_3$-SCR performance within highly $H_2O$ and $SO_2$ resistance. *Appl. Catal. B Environ.* **343**, 123442 (2024).
[70] Chen PR, *et al.* Formation and effect of $NH_4^+$ intermediates in $NH_3$–SCR over Fe-

ZSM-5 zeolite catalysts. *ACS Catal.* **6**, 7696-7700 (2016).
[71] Li R*, et al.* Remarkable performance of selective catalytic reduction of $NO_x$ by ammonia over copper-exchanged SSZ-52 catalysts. *Appl. Catal. B Environ.* **283**, 119641 (2021).
[72] Wang XF*, et al.* Insight into the effects of $Cu^{2+}$ ions and CuO species in Cu-SSZ-13 catalysts for selective catalytic reduction of NO by $NH_3$. *J. Colloid Interface Sci.* **622**, 1-10 (2022).
[73] Wang XQ*, et al.* Improving catalytic performance of Cu-SSZ-13 for $NO_x$ abatement via in-situ introduction of La and Ce from spent catalyst. *Sep. Purif. Technol.* **331**, 125638 (2024).
[74] Shen YL*, et al.* Revealing the mechanisms of $NH_3$ adsorption and reactions in catalytic $NO_x$ reduction over $Cu_X$/CHA zeolites by in situ DRIFTS spectroscopy. *Appl. Catal. B Environ.* **353**, 124094 (2024).
[75] Deringer VL*, et al.* Crystal Orbital Hamilton Population (COHP) analysis as projected from Plane-Wave basis sets. *J. Phys. Chem. A.* **115**, 5461-5466 (2011).
[76] Dronskowski R, Bloechl PE. Crystal Orbital Hamilton Populations (COHP): Energy-resolved visualization of chemical bonding in solids based on density-functional calculations. *J. Phys. Chem.* **97**, 8617-8624 (1993).

## Supplementary Files

This is a list of supplementary files associated with this preprint. Click to download.

- 2026.03.25SIRECuSSZ13npj.docx